SAND2013-4432C

Simultaneous Pressure Measurements and High-Speed Schlieren Imaging of Disturbances in a Transitional Hypersonic Boundary Layer

Katya M. Casper*, Steven J. Beresh†, Ross M. Wagnild‡, John F. Henfling§, Russell W. Spillers¶, and Brian O. M. Pruett‖

Sandia National Laboratories, Albuquerque, NM 87185

High-frequency pressure sensors were used in conjunction with a high-speed schlieren system to study the growth and breakdown of boundary-layer disturbances into turbulent spots on a 7° cone in the Sandia Hypersonic Wind Tunnel. The development of these disturbances can be clearly seen in both the schlieren images as well as the simultaneous pressure measurements. At Mach 5, intermittent low-frequency disturbances were observed in the schlieren videos. High-frequency second-mode wave packets would develop within these low-frequency disturbances and break down into isolated turbulent spots surrounded by an otherwise smooth, laminar boundary layer. At Mach 8, intermittent second-mode wave packets were observed at lower Reynolds numbers. As the Reynolds number was increased, the boundary layer was dominated by these second-mode instabilities which would break down into regions of turbulence. Second-mode waves surrounded these turbulent patches as opposed to the smooth laminar flow seen at Mach 5. At Mach 14, second-mode instability wave packets were also observed. However, only low freestream Reynolds numbers could be obtained so these waves did not break down to turbulence. These simultaneous pressure and schlieren images show the intermittent behavior of the boundary-layer over a range of Re and M. Future analysis will focus on correlating the two measurements and computing statistics of the disturbance formation that will aid in modeling transitional pressure fluctuations.

Nomenclature

δ	boundary-layer thickness (mm)	Re	freestream unit Reynolds number (1/m)
ϕ	cone azimuthal angle (°)	t	time (s)
f	camera framing rate (kHz)	T_0	tunnel stagnation temperature (K)
M	freestream Mach number	T_{aw}	adiabatic wall temperature (K)
M_e	Mach number at boundary-layer edge	T_w	wall temperature (K)
P_0	tunnel stagnation pressure (kPa)	U_c	average convection velocity (m/s)
$\tilde{p}$	root-mean-square pressure fluctuation (Pa)	U_e	boundary-layer edge velocity (m/s)
p'	pressure fluctuation, $p - p_e$ (Pa)	x	axial model coordinate measured from nose (m)
p_e	boundary-layer edge pressure (Pa)	$\tilde{x}$	axial model coordinate obtained from time-series data using Taylor's hypothesis (mm)
R	cone radius (mm)		

*Senior Member of the Technical Staff, Engineering Sciences Center, Member AIAA, kmcaspe@sandia.gov, (505) 844-1574
†Principal Member of the Technical Staff, Engineering Sciences Center, Associate Fellow AIAA
‡Senior Member of the Technical Staff, Engineering Sciences Center, Member AIAA
§Distinguished Technologist, Member AIAA
¶Senior Technologist
‖Technologist

Sandia National Laboratories is a multi-program laboratory managed and operated by Sandia Corporation, a wholly owned subsidiary of Lockheed Martin Corporation, for the U.S. Department of Energy's National Nuclear Security Administration under contract DE-AC04-94AL85000.

y spanwise model coordinate measured from top surface cone, looking upstream (mm) ($\phi = 0°$), clockwise along the circumference of the

I. Introduction

Hypersonic reentry vehicles are subjected to high levels of fluctuating pressures. These intense fluctuations can cause vibration of internal components and lead to structural problems. There is a need to predict the magnitude, frequency content, location, and spatial extent of the pressure fluctuations to better design hypersonic flight vehicles. Current designs often use overly conservative estimates of the fluctuations which lead to heavier vehicles and degraded flight performance. Some correlations exist for the magnitude of transitional and turbulent pressure fluctuations, but these were derived primarily using either incompressible data or conventional (noisy flow) hypersonic wind-tunnel tests.[1] Such modeling efforts have not led to sufficient physical understanding of the transitional pressure fluctuations or to adequate predictive capabilities. Modern computational capabilities seem likely to enable higher-fidelity models in the future.

During boundary-layer transition, the heating rates and pressure fluctuations that are experienced are higher than for a fully turbulent boundary layer.[2–6] These high pressure fluctuations result from repeated intermittent spatial-temporal switching between laminar and turbulent regions, creating a broad spectrum of disturbances. Unfortunately in flight, natural transition typically occurs over a large portion of the vehicle,[7] making transitional fluctuations of primary interest for this work. The transition process can be described through intermittency and the growth and propagation of turbulent spots in the transitional boundary layer.[8] These turbulent spots create wall pressure fluctuations. By combining the pressure fluctuations associated with wave packets and turbulent spots into a model of transition, transitional pressure fluctuations can be calculated from a physics-based simulation. This type of model has already been developed for incompressible flow on a flat plate.[9]

In order to improve prediction of hypersonic pressure fluctuations, experiments were conducted on a 7° sharp cone at zero angle of attack in two hypersonic tunnels under conventional and quiet noise levels.[10–13] Experiments under noisy flow were conducted in the Sandia National Laboratories Hypersonic Wind Tunnel (HWT) at Mach 5, 8, and 14 and in the Boeing/AFOSR Mach-6 Quiet Tunnel (BAM6QT) at Purdue University. Measurements under quiet flow were also conducted in the BAM6QT for comparison to noisy-flow measurements and flight data.

These previous measurements give an average picture of the transition process. The RMS pressure fluctuations and power spectral densities that were obtained are averages over long periods of time that might include laminar, transitional, and turbulent flow. The present work seeks intermittent data characterizing the individual disturbances that make up these averages. Simultaneous high-speed schlieren imaging and high-frequency pressure measurements were used to characterize the spatial and temporal structure of the intermittent disturbances. The present results show selected individual disturbances over a variety of freestream Mach numbers and Reynolds numbers. Accelerometers were also mounted on the model and tunnel in order to characterize the vibration environment of the cone. Correlations between these accelerometers and pressure measurements were explored to prepare for future experiments studying fluid-structure interactions caused by the transitional pressure loading.

Future work will focus on quantitatively correlating the schlieren and pressure measurements. Also, the statistics of these individual disturbances will be computed, providing the burst rate, distribution of burst length, and boundary-layer intermittency along the cone. These statistics can be combined with the pressure structure and growth rate of these spots obtained from previous work[14] to model the transitional pressure fluctuations. These models can then be compared to the average RMS pressure fluctuation measurements along the cone[10, 12, 13] and then be extended for predicting a flight vehicle's environment.

II. Experimental Setup

A. Sandia Hypersonic Wind Tunnel

The Sandia Hypersonic Wind Tunnel (HWT) is a conventional blowdown-to-vacuum facility. Interchangeable nozzle and heater sections allow the tunnel to be run at Mach 5, 8 or 14. Run times were typically 30 s. Mach 5 tests use air as the driver gas. HWT-5 has a P_0 range of 345–1380 kPa and a T_0 range of 330–890 K, giving a Re range of 3.3–26 $\times 10^6/m$. Noise levels vary from 1–2% in this tunnel.[10] HWT-8 uses 689 MPa

nitrogen supplied from a bottle farm. It has a P_0 range of 1720–6890 kPa, T_0 range of 500–890 K, and Re can be varied from 3.3–$20 \times 10^6/m$. Noise levels vary from 3–5%.[10] HWT-14 also uses the nitrogen system. The total pressure and temperature can be varied from 4830–20.7 MPa and 940–1400 K, respectively. This gives a Re range of 1.3–$4.0 \times 10^6/m$. Tunnel noise has not been characterized at Mach 14.

Freestream conditions in this tunnel are computed using the Beattie-Bridgeman model to account for real-gas effects. At the low freestream temperatures in these tunnels, a linear viscosity law is used. Edge conditions used for normalization of the data were computed using a Taylor-Maccoll solution for flow over the cone.

B. High-Speed Schlieren System

A high-speed schlieren system was developed to take images at a high frequency while also being able to resolve the detailed structure of the boundary-layer disturbances. Fig. 1 shows a simple schematic of the final system design. Figs. 2(a) and 2(b) show pictures of the setup.

The light source was a Flashpoint II 1220A Monolight which emits white light. This light has a flash energy rating of 600 Watt-s and a flash duration between 1–2 ms. The light could be fired every 2.5 seconds, allowing ten short movies to be captured during a typical run. Several hundred usable images were captured per movie. The exact number depended on the image resolution and frame rate for a given run. The light from the source was passed through a slit to increase sensitivity and provide a more well-defined effective source. Two 101.6-mm diameter convex lenses with a 1-m focal length were then used to collimate the remaining light, pass it through the test section, and focus the light on a knife edge. The lenses were equally spaced on either side of the tunnel centerline. Most of the light was cutoff at the knife edge in order to increase the sensitivity of the schlieren system. The remaining light was then passed to a Phantom v12.1 digital camera. The slit, knife edge, and camera were all tilted 7° from horizontal to line up with the cone surface.

The Phantom camera was used for its high light sensitivity, fast imaging capabilities, and short exposure time. The camera has a fill factor of 56% and a 20 μm pixel size. The minimum exposure time of 285 ns was used for all images. The lens used with the camera was varied between a 85, 105, and 180-mm lens with f-stops of f/1.8, f/2.8, and f/3.5, respectively. The 180-mm lens was typically used at Mach 5 to give better resolution in the thin boundary layer. The 105-mm lens was used instead for Mach 8 and 14; resolution was sacrificed in order to retain more light needed at the lower freestream densities at higher M. The exact resolution and framing rate was varied from run to run.

The schlieren images integrate through a curved boundary layer which will have some effect on the data. The maximum azimuthal integration length at the middle of the schlieren viewing area was estimated by calculating the length of the circular segment at the radius of the cone R plus the boundary layer thickness δ, at a height R. At Mach 5 at a Re near $4.0 \times 10^6/m$, the boundary layer thickness is approximately 1.5 mm as determined optically from the schlieren images. This gives a maximum azimuthal integration length of approximately 15 times the boundary-layer thickness. At Mach 8 at a similar Re, the maximum azimuthal integration length is approximately 13 δ (δ is approximately 2.3 mm). At Mach 14, the boundary layer is approximately 3.4 mm thick near this Re, giving an azimuthal integration length of 10 δ.

Images were post-processed by applying a flat-field correction. The images were then contrast enhanced to emphasize the boundary-layer disturbances; the top 0.1% of the images was saturated and a gamma correction ($\gamma = 1.5$) was applied to nonlinearly weight the images towards darker values.

C. Model and Instrumentation

A 0.517-m-long 7° half-angle stainless-steel cone was used for this work (Fig. 3(a)). This cone has been used in previous experimental campaigns.[10–13] Two new inserts were fabricated to place closely spaced axial and spanwise arrays of pressure sensors on the cone. The axial array (Fig. 3(b)) has five PCB132 pressure sensors spaced 5.1 mm apart. The fourth PCB132 sensor at x = 0.386 m was not working for these tests. The schlieren viewing area was centered around this axial array (between x = 0.326 and 0.416 m) to allow simultaneous schlieren imaging and high-frequency pressure measurements. The spanwise array of sensors was located downstream of the schlieren viewing area at x = 0.452 m. Thirteen PCB132 sensors were spaced between 5 and 10 degrees apart in this array. Tables 1 and 2 list the location of the pressure sensors and the schlieren viewing area. A sharp nose (radius less than 0.05 mm) was used for these tests.

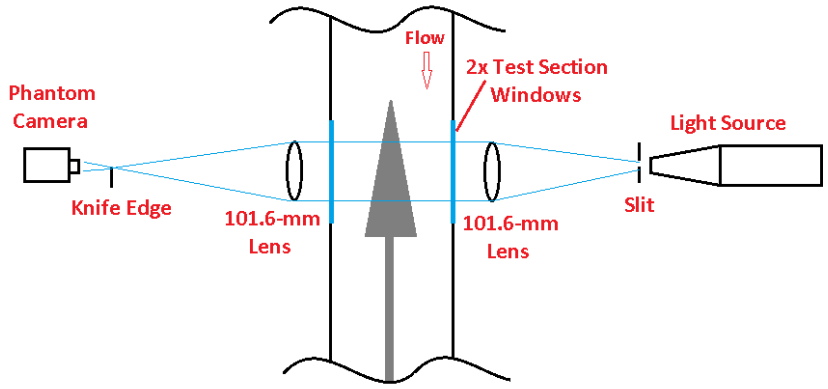

Figure 1. Schematic of the high-speed schlieren system developed for the Sandia Hypersonic Wind Tunnel.

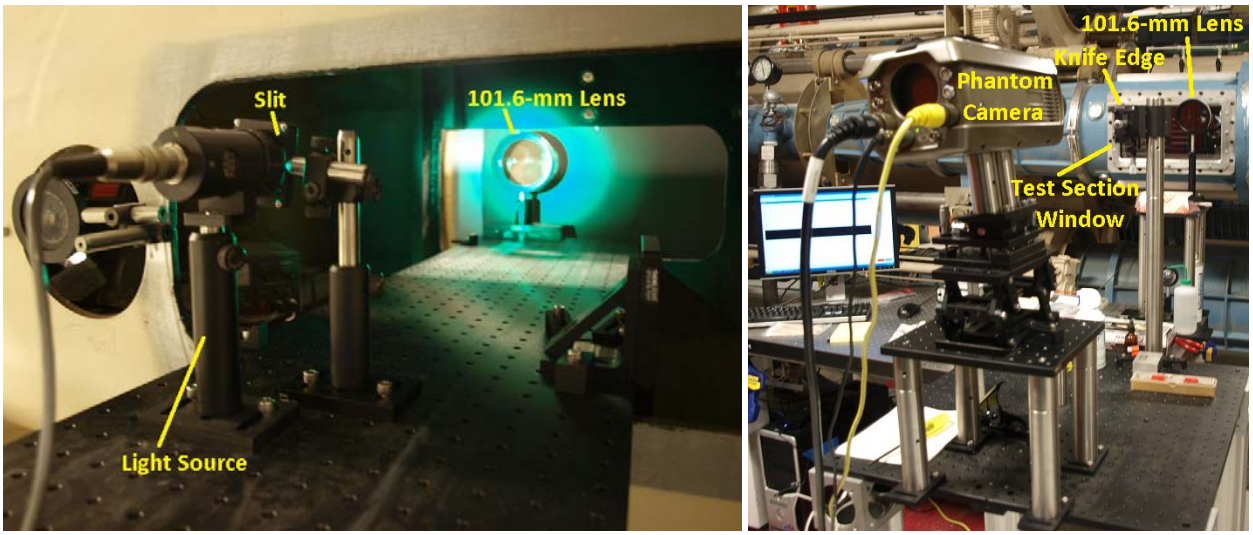

(a) (b)

Figure 2. High-speed schlieren system. The LED light source used for alignment is shown in place of the Flashpoint Monolight.

Additional instrumentation was also used to begin studying coupled fluid-structure interactions resulting from boundary-layer transition. A Kulite Mic-062 sensor was placed on the base of the cone to measure base pressure fluctuations. Also, several accelerometers were used to characterize the model vibration environment. A PCB356A03 triaxial accelerometer was placed on the tunnel test-section outer wall. Three additional Endevco 66A50 triaxial accelerometers were placed on the model sting, on the inside base of the model, and on the inside of the model between the axial and spanwise pressure sensor arrays.

Two types of sensors were used to measure the pressure fluctuations. Kulite Mic-062 A-screen sensors are used to measure fluctuations between 0 and 50 kHz. These microphones measure the pressure differential across a diaphragm, up to ± 7 kPa. The back side of the diaphragm has a pressure reference tube that is approximately 0.05 m long. This tube was left open to the plenum inside of the model which gives an approximately steady reference pressure. The diameter of these sensors is 1.59 mm. They have a nominal resonant frequency of 125 kHz and a nominal sensitivity of 0.207 mV/Pa. The quoted repeatability of the sensors is approximately 0.1% of the full scale, or 7 Pa. For these tests, only A-screen sensors were used. The A-screen has a large central hole. This screen offers only a small amount of diaphragm protection, but the sensor has a flatter frequency response up to 30–40% of the resonant frequency.[15] The sensitive area of the A-screen sensor is the hole size (0.81 mm^2).

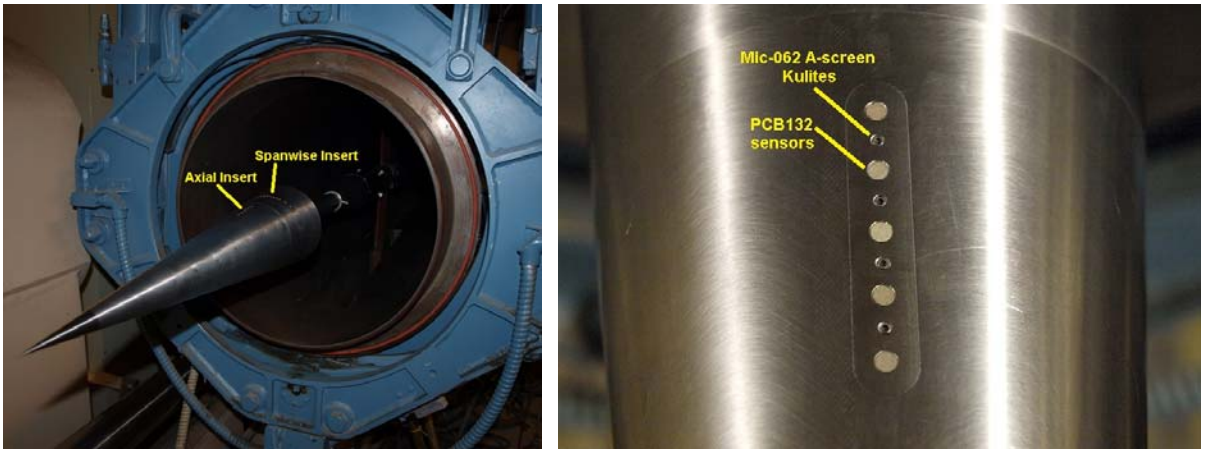

(a) (b)

Figure 3. Wind-tunnel model (a) Cone installed in the Sandia Hypersonic Wind Tunnel; (b) Close-up view of the axial insert showing closely spaced pressure instrumentation.

Table 1. Axial location of schlieren viewing area and PCB132 pressure sensors on 7° cone.

Location	Sensor	$\phi(^\circ)$	x (m)
Beginning of Schlieren Viewing Area			0.326
A1	PCB132	0	0.355
A3	PCB132	0	0.365
A5	PCB132	0	0.376
A7	PCB132	0	0.386
A9	PCB132	0	0.396
End of Schlieren Viewing Area			0.416
Spanwise Insert	PCB132		0.452

Table 2. Spanwise location of PCB132 pressure sensors on the 7° cone.

Location	Sensor	$\phi(^\circ)$	y (mm)
S1	PCB132	-40	-38.7
S2	PCB132	-30	-29.1
S3	PCB132	-20	-19.4
S4	PCB132	-15	-14.5
S5	PCB132	-10	-9.7
S6	PCB132	-5	-4.8
S7	PCB132	0	0.0
S8	PCB132	5	4.8
S9	PCB132	10	9.7
S10	PCB132	15	14.5
S11	PCB132	20	19.4
S12	PCB132	30	29.1
S13	PCB132	40	38.7

The growth and breakdown of the second-mode instability leading to transition can be studied with PCB132 sensors. The PCB132's can measure pressure fluctuations between 11 kHz and 1 MHz. The sensor is a very high frequency piezoelectric time-of-arrival sensor. The resonant frequency is above 1 MHz; however, the sensor output is high-pass filtered at 11 kHz, per the manufacturer's specifications. The sensors allow a study of instability breakdown to transition and are useful indicators of transition on the model. Also, the sensors have adequate frequency response to resolve the short duration of turbulent spots on the cone. However, the amplitude response of the sensors has not yet been accurately calibrated. In addition, the sensors have spatial resolution limitations. Second-mode waves have a wavelength of approximately twice the boundary-layer thickness (δ is about 1–3 mm for measurements on a typical cone model). The PCB132 diameter (3.18 mm) is larger than half of the instability wavelength on the cone. The actual sensitive area of the face is smaller, but its exact area is unknown. Some initial calibration work has been completed,[15,16] but more in-depth calibration is still needed. A shock tube has recently been built at Purdue for these purposes.[17]

Triaxial accelerometers were used to characterize the vibration environment of the cone. The PCB356A03 is a miniature ICP type triaxial accelerometer. It has a resonant frequency above 50 kHz. It can resolve frequencies between 2–5000 Hz on its x axis and between 2–8000 Hz on the y or z axes. Its sensitivity is 10 mV/g. The Endevco 66A50 accelerometers have a slightly better performance. They have a resonant frequency of 55 kHz and can resolve frequencies between 0.4–14000 Hz on all axes. Their sensitivity is 5 mV/g.

D. Data Acquisition

Kulite sensors need an excitation voltage for operation. A 10 V excitation is applied using an Endevco Model 136 DC Amplifier. The amplifier was also used to supply a gain of 100 for Kulite signal output. A Krohn-Hite Model 3384 Tunable Active Filter was used as an anti-aliasing low-pass Bessel filter. The filter was set at 75 kHz, has eight poles, and provides 48 dB attenuation per octave. The Kulite sampling frequency was 500 kHz. The PCB132 sensors all run through a PCB 482A22 signal conditioner that provides constant-current excitation to the built-in sensor amplifier. It also decouples the AC signal from the DC bias voltage. The output from the signal conditioner is fed through a Krohn-Hite Model 3944 Filter with a 1.25 MHz low-pass anti-aliasing Bessel filter. This filter has four poles and offers 24 dB of attenuation per octave. The sampling frequency for the PCB132 sensors was 2.5 MHz. Pressure sensor data was acquired using a National Instruments PXI-1042 chassis with 14-bit PXI-6133 modules (10 MHz bandwidth). Accelerometer data was acquired using a CDAQ-9188 chassis and 24-bit NI-9232 analog input modules. These modules have built-in anti-aliasing filters. Accelerometer data were acquired at the maximum rate of 102.4 kHz. Ten 0.2 second segments of data were acquired every 2.5 seconds during each run. These segments were triggered by a Stanford Research Systems DG645 Digital Delay Generator that also simultaneously triggered the light source and camera of the schlieren system.

III. Stability Computations

Boundary-layer stability computations were performed to look at the relative dominance of first and second-mode instabilities in the HWT and compare to the pressure and schlieren measurements. These computations are similar to previous computations on the cone.[12] The mean flow for the stability analysis is calculated using a structured-grid, axi-symmetric CFD solver, which solves the reacting Navier-Stokes equations and is part of the STABL software suite.[18] This flow solver is also based on the finite-volume formulation. The inviscid fluxes are calculated using the modified Steger-Warming flux vector splitting method and are second-order accurate with a MUSCL limiter as the TVD scheme. The viscous fluxes are second-order accurate. The time advancement method is the implicit, first-order DPLR method. The mean flow is computed on a single-block, structured grid with dimensions of 450 cells by 350 cells in the streamwise and wall-normal directions, respectively. The grid is clustered at the wall as well as at the nose in order to capture the gradients in these locations. In calculations of HWT-5, a single species, non-reacting gas composed of air is used to model the fluid. In calculations of the Mach 8 and Mach 14 tunnels, a single-species, non-reacting gas composed of N_2 is used to model the fluid.

The stability analyses are performed using the PSE-Chem solver, which is also part of the STABL software suite. PSE-Chem[19] solves the reacting, two-dimensional, axi-symmetric, linear parabolized stability

equations to predict the amplification of disturbances as they interact with the boundary layer. The PSE-Chem solver includes finite-rate chemistry and translational-vibrational energy exchange. The parabolized stability equations predict the amplification of disturbances as they interact with the boundary layer.

IV. Experimental Results

A. HWT-5

Simultaneous schlieren and pressure measurements were made at Mach 5 over a range of freestream Reynolds numbers. At a low Reynolds number of $4.39 \times 10^6/m$, the boundary layer is predominately laminar over the schlieren viewing area. Fig. 4 shows a typical schlieren image at this condition. The red arrows mark the location of four PCB132 sensors beneath the viewing area at x = 0.355, 0.365, 0.376, and 0.396 m. The boundary layer is smooth and thin and no disturbances are seen propagating through the boundary layer. Fig. 5(a) shows the corresponding pressure traces from the four PCB132 sensors. The time of the schlieren image is shown with a vertical black line. The traces are offset from each other proportional to their axial location on the cone in order to show the growth and convection of boundary-layer disturbances. These traces, however, show no evidence of large disturbances. Only small low-frequency content is observed. Power-spectral densities (PSD's) were computed from these 200 μs pressure traces using a blackman window. Because only a single time trace is used for the computation, the plots are noisy (there is no averaging). Also, because of the short time traces used, the resolution of the spectra is only 5 kHz. However, the spectra can still indicate the frequency of the boundary-layer disturbances. In this case, there is some low-frequency content in the signal, but the boundary layer appears smooth and laminar.

Further downstream at x = 0.452 m, small, intermittent wave packets are observed in the pressure traces. The peak frequency of these wave packets is near 220 kHz. STABL computations were performed to identify these waves. For cones in hypersonic flow at zero angle of attack, the dominant boundary-layer instability is the second-mode instability. This instability acts like a trapped acoustic wave in the boundary layer, so the frequency of the second-mode waves is inversely proportional to the boundary-layer thickness. The most amplified waves are two-dimensional. In HWT-5, the edge Mach number M_e is near 4.3, which is low for second-mode instability dominance. Instead at supersonic edge Mach numbers, the first mode instability tends to dominate. First-mode waves have the largest growth at oblique angles. At x = 0.452 m, the STABL computations indicate second-mode waves with a maximum N factor of 2.6. This N factor quantifies how much a disturbance has grown from its initial amplitude. This maximum growth occurs for a disturbance with a frequency of 224 kHz which is in good agreement with the frequency of the waves observed in the experiments. It is interesting to note that in HWT-5, stability computations predict significant amplification of first-mode waves. Mid-way through the schlieren viewing area at x = 0.376 m, the computations indicate a maximum second-mode N factor of 2.2 with a frequency of 240 kHz. The first-mode instability actually has a comparable N factor of 1.5 at a frequency of 27 kHz and a wave angle of 58 degrees. However at this Re, the boundary layer remains laminar in the schlieren viewing area, so these disturbances are not observed.

In order to show the three-dimensional structure of the disturbances, pressure traces from the spanwise array of sensors at x = 0.452 m were converted into a contour plot of the pressure field. Time traces of the pressure fluctuations at each y location were converted to an approximate streamwise coordinate $\tilde{x}$ using an average disturbance convection velocity ($\tilde{x} = -tU_c$). An average convection velocity of 0.8 U_e was used, which is in agreement with previous measurements on a cone.[13,14] The zero time origin for each case was picked in order to align the leading edges of the dominant disturbance at $\tilde{x} = 0$ m. This conversion invokes Taylor's hypothesis which assumes the flow is 'frozen' as it convects over the sensor.[20] This hypothesis is frequently used in the analysis of turbulent flow and has been shown to be a reasonable assumption for many cases, even for low-frequency fluctuations.[21] In the present case, the disturbances will grow in length as they convect over the sensors, but this conversion allows a reasonable approximation of the spatial footprint of the disturbances to be studied. When the time traces are converted to distance, a smaller time corresponds to a greater $\tilde{x}$ location. As a result, the front or leading edge of the disturbance corresponds to smaller t and larger $\tilde{x}$ while the rear or trailing edge corresponds to larger t and smaller $\tilde{x}$.

Fig. 6 shows the resulting contour plot. Small wave packets with peak fluctuation amplitudes of only 0.3 p_e are observed. The wave packets are narrow and are only observed in at most two adjacent PCB132 sensors. This is in agreement with measurements by Kimmel[22] under conventional noise levels that showed that the spanwise coherence of the second-mode waves was only 4 δ. In this case, 4 δ extends to only 6 mm, which would reach a maximum of two PCB132 sensors. A more dense array of much smaller diameter

sensors would be needed to better resolve the structure of these disturbances.

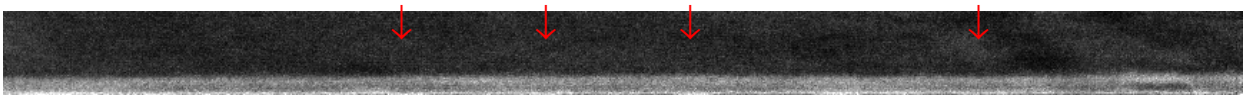

Figure 4. Schlieren image showing laminar flow, HWT-5, $t = 1.131\ ms$, $Re = 4.39 \times 10^6/m$, $M = 4.95$, $P_0 = 376.3\ kPa$, $T_0 = 528\ K$.

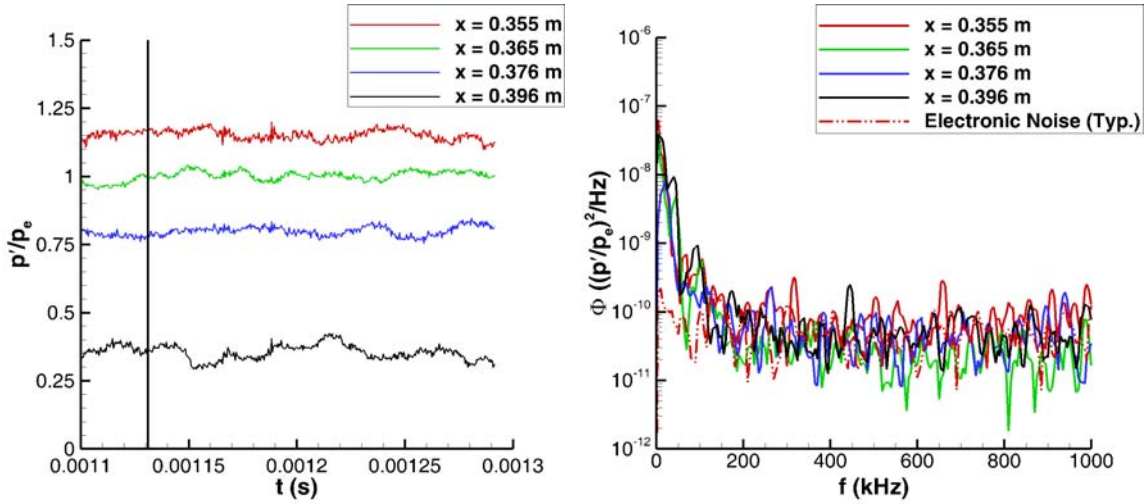

(a) (b)

Figure 5. Simultaneous pressure measurements, HWT-5, $Re = 4.39 \times 10^6/m$, $M = 4.95$, $P_0 = 376.3\ kPa$, $T_0 = 528\ K$ **(a) Pressure traces, each trace is vertically offset proportional to x. A vertical black line marks the time of the corresponding schlieren image; (b) Power-spectral densities.**

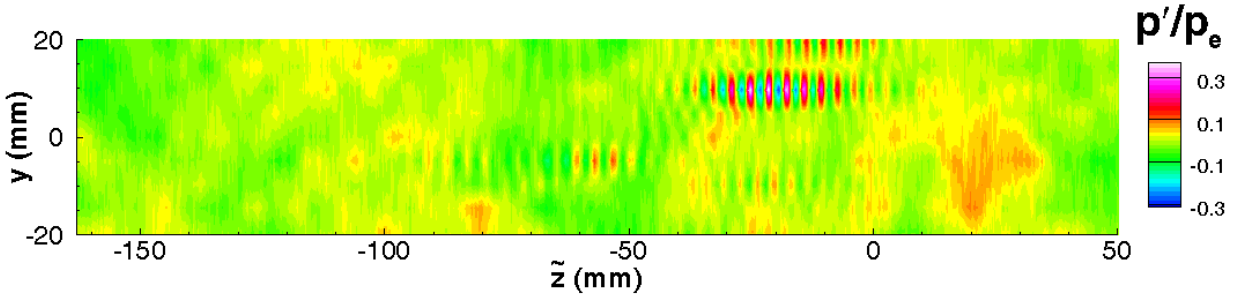

Figure 6. Contour plot showing intermittent wave packets, HWT-5, $Re = 4.39 \times 10^6/m$, $M = 4.95$, $P_0 = 376.3\ kPa$, $T_0 = 528\ K$.

At a higher Re of $8.98 \times 10^6/m$, intermittent disturbances form within the laminar boundary layer. Fig. 7 shows subsequent schlieren images of one intermittent disturbance as it forms and breaks down over the schlieren viewing area. At first, a low-frequency disturbance is seen near the center of the images. The frequency of this disturbance was estimated from the schlieren images. The leading and trailing edges of the disturbance were chosen at different points through the boundary layer. An average convection velocity of 0.8 U_e was then used to convert the spatial distance between subsequent wave peaks to an estimated frequency. This frequency varied from 40–52 kHz through the boundary layer. As the disturbance convects downstream, periodic higher frequency disturbances can be seen growing inside of the low-frequency disturbance. These disturbances show a typical rope-like structure as expected for second-mode waves. However, in this case they appear to form diagonally through the boundary layer, on top of the low-frequency disturbance. Typical

second-mode wave schlieren images show the disturbances as rope waves at a constant height near the boundary-layer edge.[23] The frequency of these higher-frequency disturbances was again estimated from the schlieren images by picking subsequent wave peaks. This frequency decreased from 390 kHz at the trailing edge of the packet to 210 kHz at the leading edge.

Simultaneous pressure traces and the corresponding power-spectral densities are shown in Fig. 8. At the first two sensor locations, only low-amplitude, low-frequency oscillations are seen. The boundary layer remains laminar at these locations, in agreement with the schlieren images. The low-frequency disturbance seen in the schlieren images before high-frequency disturbances develop is not evident in the surface pressure measurements. By the last two sensor locations, the boundary-layer disturbances are evident. A large pressure spike and higher frequency oscillations are observed at x = 0.376 m, followed by larger oscillations at x = 0.396 m. The power-spectral density show a peak in the spectra near 200 kHz at x = 0.376 m, followed by more broadband frequencies at x = 0.396 m. Unfortunately, the wave packet nature of this disturbance is not captured with this sensor spacing, but other examples better show the high-frequency wave packets (Fig. 10(a)).

STABL computations were again performed to look at the growth of the first and second-mode instabilities in this flow. The computations show that both instabilities have nearly equal N factors. In the middle of the schlieren viewing area at x = 0.376 m, the second-mode instability has a maximum N factor of 3.6 at a frequency of 297 kHz. The first mode is actually more amplified and has an N factor of 4.1. Its dominant frequency is 44 kHz and occurs at a wave angle of 50 degrees. The high-frequency disturbances observed in the schlieren show reasonable agreement with the second-mode stability computations. The low-frequency disturbance also has a frequency in good agreement with a first-mode wave. However, it is not known how an oblique disturbance would show up in a schlieren image. It will later be shown in Section B that at higher Mach numbers, this low-frequency disturbance is not observed. The maximum second-mode N factors are also significantly larger than the maximum first-mode N factors at both Mach 8 and 14. This seems to indicate that this low-frequency disturbance at Mach 5 could be the first-mode instability, but more evidence is need to to conclusively identify this disturbance.

At a higher Re of $9.75 \times 10^6/m$, disturbances again form intermittently in the boundary layer. However, the disturbances tend to form and break down to turbulent spots further upstream (Fig. 9). In this case, a low-frequency disturbance is again seen convecting within a smooth, laminar boundary layer (Figs. 9(a) – 9(b)). Higher frequency periodic waves again develop on top of this low-frequency disturbance (Figs. 9(c) – 9(d)). This disturbance then breaks down into a turbulent spot that continues to convect and grow downstream. Fig. 10 shows simultaneous pressure traces and the corresponding PSD's for this case. The first sensor shows the large high-frequency waves passing by the sensor, in agreement with the schlieren images. However, the low-frequency disturbance is not seen in the traces. The PSD's show a peak in the spectra between 200 and 400 kHz, at a range expected for the second-mode instability. The last three sensor locations show a turbulent disturbance passing by the sensors, in agreement with the schlieren images. The spectra also indicates mores broadband frequencies.

These intermittent results can be compared to the average PSD's computed over much longer time intervals. Fig. 11 shows power-spectral densities computed from a 0.2 s portion of the run. A blackman window, 5000 point window segments, and 50 % overlap were used in the computation, giving a spectral resolution of 500 Hz. The resulting spectra are much smoother than the spectra of individual disturbances since they are an average over many window segments. These average PSD's show the gradual evolution of the spectra throughout transition, as more and more intermittent disturbances develop downstream. The first three sensor locations show broad peaks between 200–400 kHz. These correspond to the presence of intermittent second-mode waves in the time traces. The only difference between the spectra is an increase in broadband frequencies between 50–150 kHz. By x = 0.396 m, more broadband frequencies have developed, indicating that the flow is more turbulent at this location. However, the peak corresponding to the second-mode waves is still present indicating that the flow is not yet fully turbulent at this location. By x = 0.452 m, the flow appears fully turbulent and evidence of intermittent second-mode waves is no longer present. These results are different than the individual spectra shown in Fig. 10(b). The individual disturbance is already turbulent by x = 0.365 m, so the individual spectra indicate broadband frequencies. Also, by x = 0.396 m, the average spectra indicate much higher levels of broadband frequency content, especially around 100 kHz corresponding to the intermittent development of boundary-layer disturbances. These elevated frequencies are not seen in the individual spectra because only a single disturbance is used in the computation.

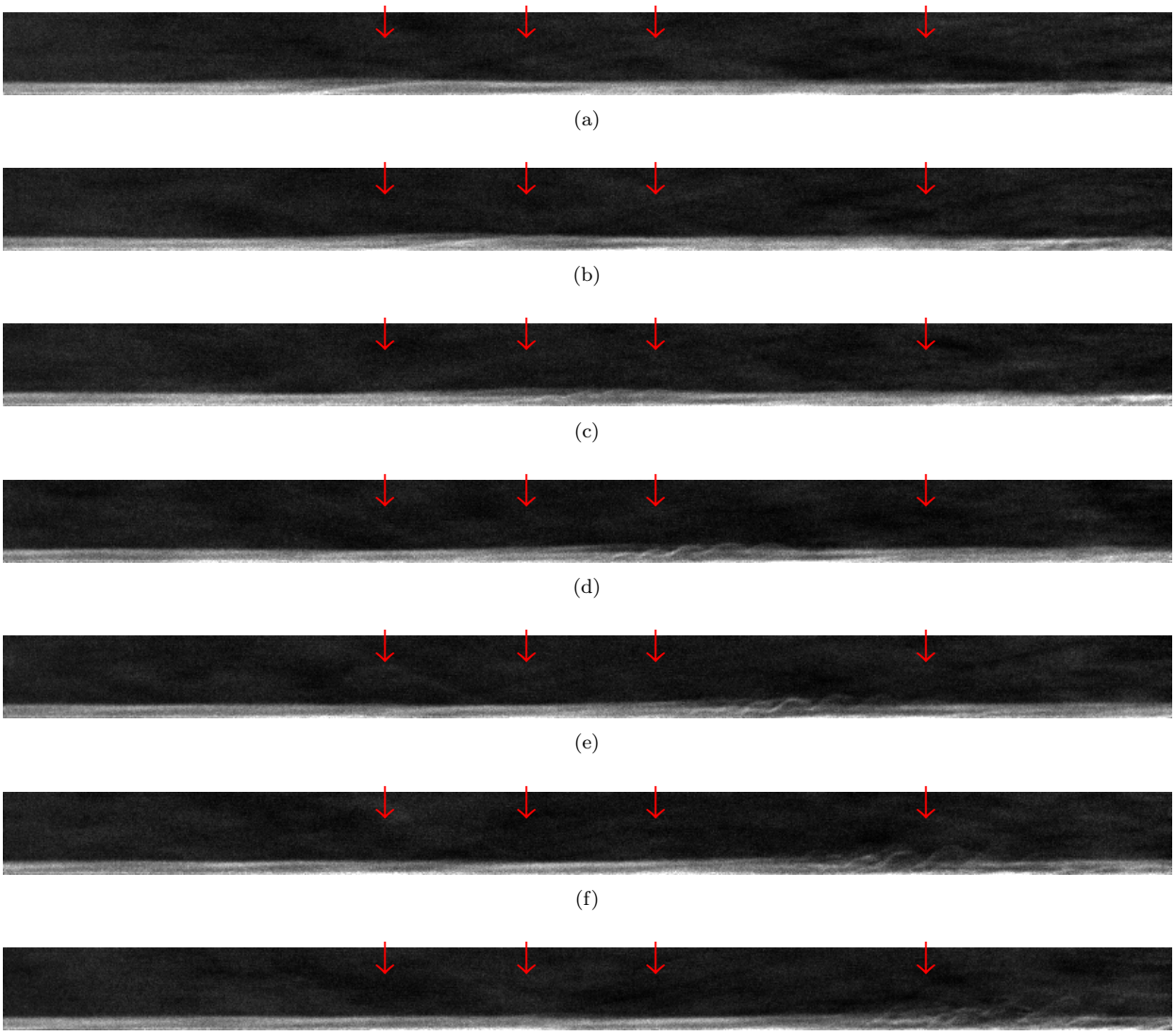

(a)

(b)

(c)

(d)

(e)

(f)

(g)

Figure 7. Schlieren images showing intermittent disturbances within mostly laminar flow, HWT-5, $t = 0.769 - 0.835ms$, $f = 91\ kHz$, $Re = 8.98 \times 10^6/m$, $M = 4.96$, $P_0 = 577.3\ kpa$, $T_0 = 435.8\ K$.

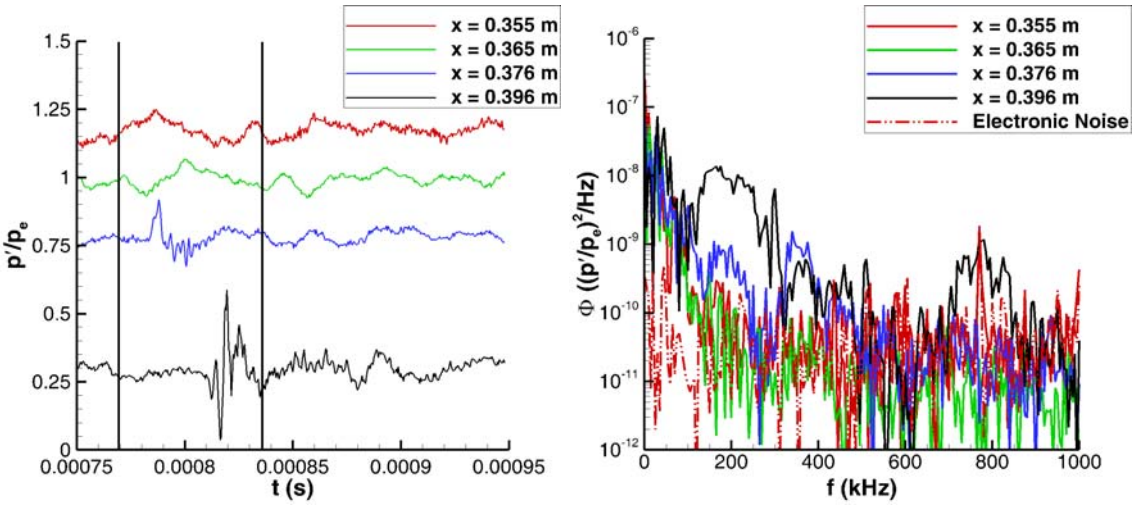

(a) (b)

Figure 8. Simultaneous pressure measurements, HWT-5, $Re = 8.98 \times 10^6/m$, $M = 4.96$, $P_0 = 577.3\ kpa$, $T_0 = 435.8\ K$ **(a) Pressure traces, each trace is vertically offset proportional to x. Vertical black lines mark the time of the corresponding schlieren images; (b) Power-spectral densities.**

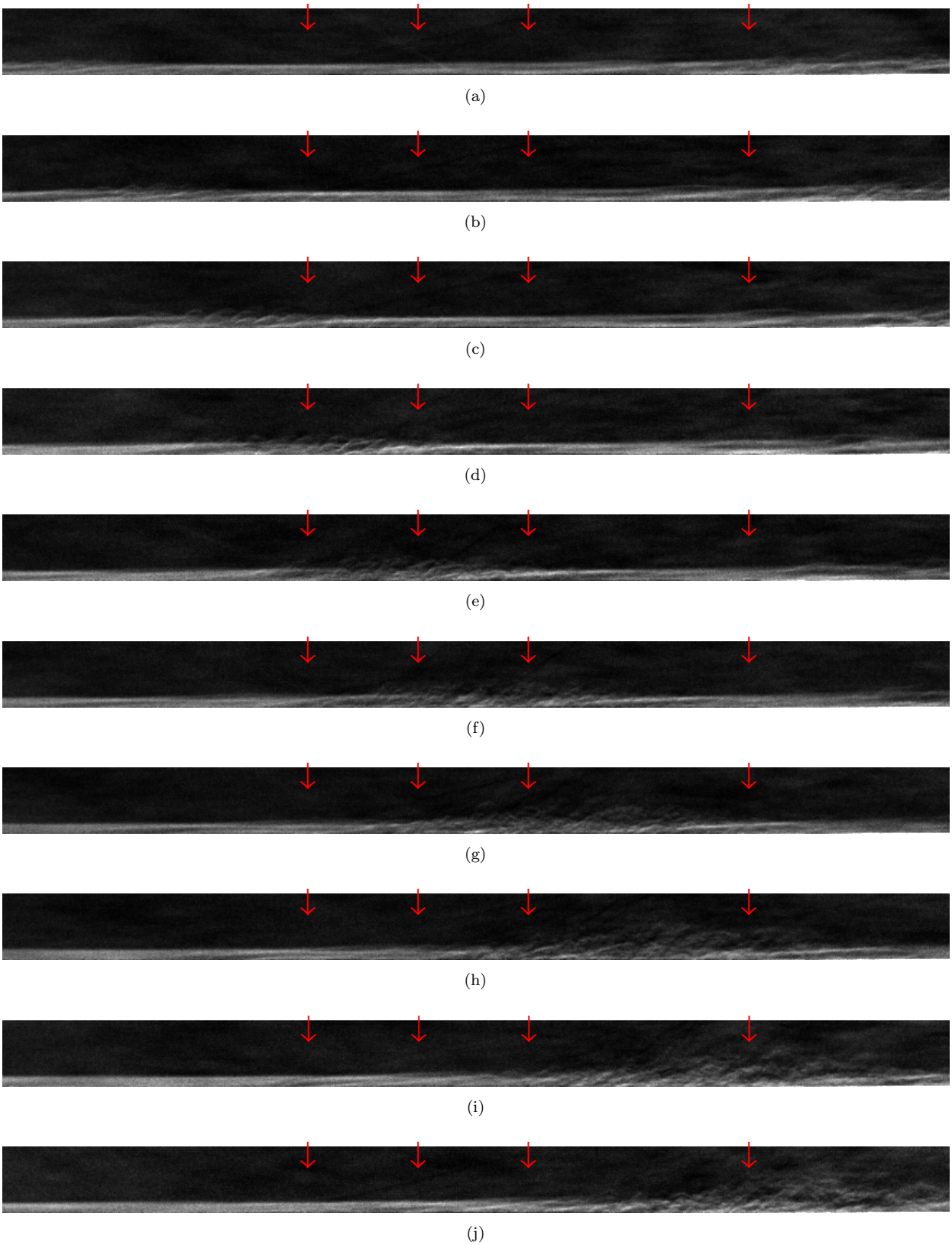

Figure 9. Schlieren images showing intermittent disturbances within mostly laminar flow, HWT-5, $t = 0.670 - 0.769\ ms$, $f = 91\ kHz$, $Re = 9.75 \times 10^6/m$, $M = 4.96$, $P_0 = 650.3\ kpa$, $T_0 = 446.6\ K$.

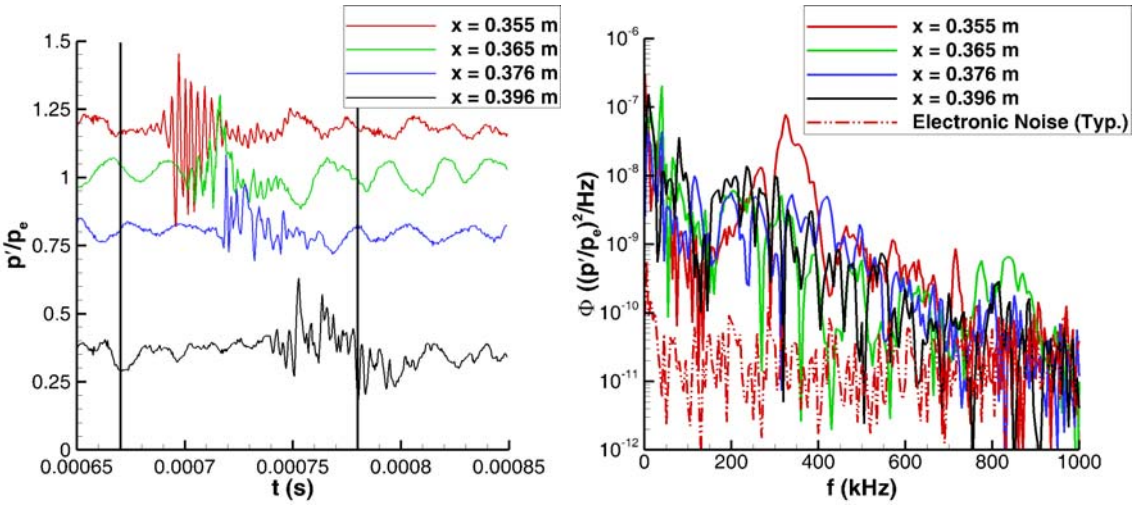

(a) (b)

Figure 10. Simultaneous pressure measurements, HWT-5, $Re = 9.75 \times 10^6/m$**,** $M = 4.96$**,** $P_0 = 650.3\ kpa$**,** $T_0 = 446.6\ K$ **(a) Pressure traces, each trace is vertically offset proportional to x. Vertical black lines mark the time of the corresponding schlieren images; (b) Power-spectral densities.**

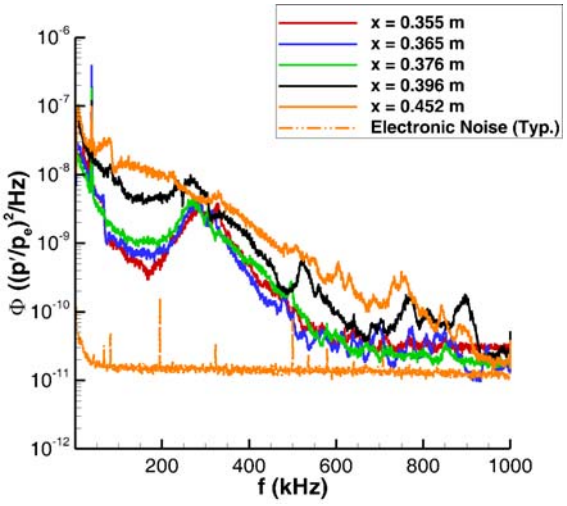

(a)

Figure 11. Average PCB132 power-spectral densities, HWT-5, $Re = 9.75 \times 10^6/m$**,** $M = 4.96$**,** $P_0 = 650.3\ kpa$**,** $T_0 = 446.6\ K$**.**

B. HWT-8

Simultaneous schlieren and pressure measurements were also obtained at Mach 8 over a range of Re. Fig. 12 shows a schlieren image at a similar low Re to the Mach 5 case in Fig. 4. Small second-mode wave packets are observed in the schlieren viewing area, instead of the smooth, laminar boundary layer seen at Mach 5. Fig. 13 shows pressure traces and power-spectral densities corresponding to the four sensor locations marked in the schlieren image. The pressure traces appear to show a small offset from the schlieren images. Several cycles of the wave packet have passed by the first three sensors, but the time traces, especially at x = 0.376 m, do not show as many oscillations. This time offset was not seen at Mach 5 and should be investigated further as correlations between the schlieren and pressure measurements are developed. The spectra show a large peak in the spectra near 200 kHz, as well as a second peak that is forming near 400 kHz. STABL computations show that the dominant second-mode waves at x = 0.376 m have a frequency of 185 kHz and reach an N factor of 4.1. In this case, low-frequency disturbances preceding the formation of the wave packets are not observed. STABL computations show that the maximum N factor for the first mode is 0.6 at a frequency of 36 kHz and a wave angle of 66 degrees. This first-mode N factor is much lower than second-mode N factor and would not be expected to be observed.

A contour plot of pressure traces obtained from the spanwise array of sensors further downstream at x = 0.452 m is shown in Fig. 14. These wave packets are similar in shape to what was observed at Mach 5, though the frequency is lower because of the thicker boundary layer. The wave packets also tend to have a wider spatial extent as expected.

Figure 12. Schlieren images showing intermittent second-mode wave packets, HWT-8, $t = 0.420\ ms$, $Re = 3.62 \times 10^6/m$, $M = 7.8$, $P_0 = 2015\ kPa$, $T_0 = 831\ K$.

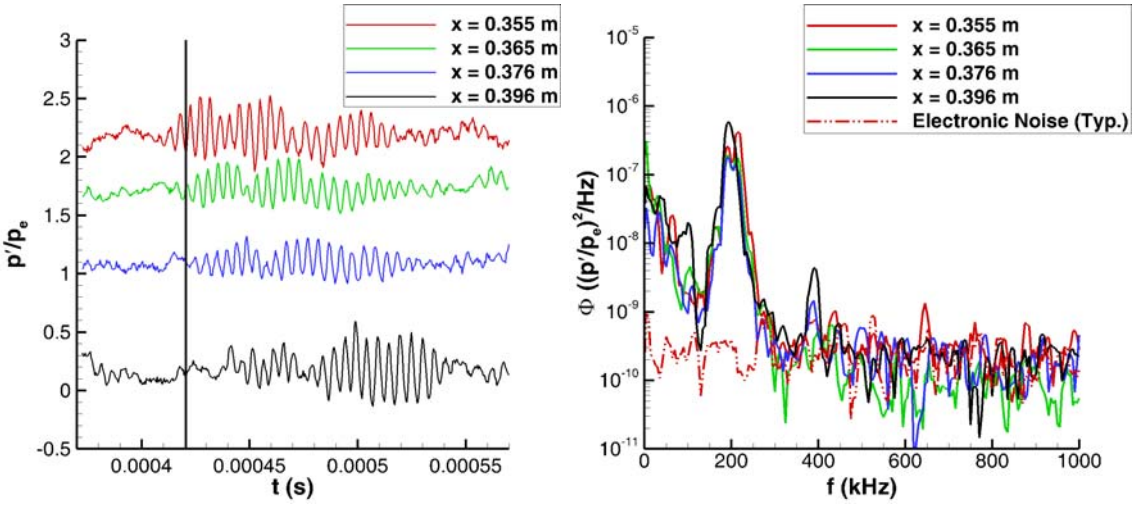

(a) (b)

Figure 13. Simultaneous pressure measurements, HWT-8, $Re = 3.62 \times 10^6/m$, $M = 7.8$, $P_0 = 2015\ kPa$, $T_0 = 831\ K$ **(a) Pressure traces, each trace is vertically offset proportional to x. A vertical black line marks the time of the corresponding schlieren image; (b) Power-spectral densities.**

At a higher Re of $7.08 \times 10^6/m$, second-mode waves dominate the flow and are observed throughout the schlieren viewing area. Patches of the waves distort and appear to begin to break down to turbulence, but second-mode waves are still observed on either side of this region. A typical schlieren example is shown in Fig. 15. A patch of distorted waves is observed at the left of Fig. 15(d). This patch convects and grows downstream in subsequent images and appears to become turbulent by Fig. 15(j). Behind this patch, second-mode waves are again observed. Fig. 16(a) shows the corresponding pressure traces. Large second-mode

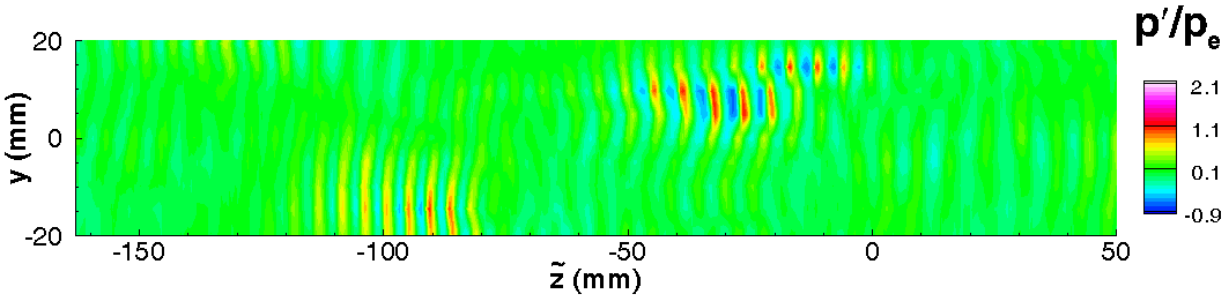

Figure 14. Contour plot showing intermittent wave packets, HWT-8, $Re = 3.62 \times 10^6/m$, $M = 7.8$, $P_0 = 2015\ kPa$, $T_0 = 831\ K$.

waves are observed, but by x = 0.396 m, some of these waves are beginning to resemble turbulent fluctuations. The PSD's show a peak near 200 kHz in the spectra corresponding to the second-mode waves (Fig. 16(b)). By x = 0.396 m, the spectra is beginning to fill in near 100 kHz as some turbulence develops.

At a higher Re of $9.74 \times 10^6/m$, larger patches of turbulent flow have developed, but these are still surrounded by second-mode instability waves (Fig. 17). The simultaneous pressure traces appear mostly turbulent, with only small regions of periodic second-mode waves (Fig. 18(a)). The corresponding PSD's show broadband frequencies indicating mostly turbulent flow (Fig. 18(b)). This is a similar Re to the Mach 5 case shown in Fig. 9. However at Mach 5, isolated wave packets and turbulent spots were observed within an otherwise smooth, laminar boundary layer.

C. HWT-14

Simultaneous high-frequency pressure and schlieren measurements were also made in HWT-14. However, the Re range of the tunnel is limited; the maximum Re in HWT-14 is similar to the lowest Re tested in HWT-5 and 8. Figs. 19 show typical schlieren images and simultaneous pressure measurements at this Re. An intermittent wave packet is seen as it propagates downstream. Fig. 20(a) shows the corresponding pressure measurements. In this case, there seems to be a timing difference between the schlieren images and surface pressure measurements. The wave packet seems to pass by in the schlieren images before the disturbances are measured on the surface. This offset was not observed at Mach 5 and was much smaller at Mach 8. Further investigation of this is needed as the schlieren and pressure measurements are correlated. The spectra of these traces show that the frequency of these wave packets is approximately 135 kHz (Fig. 20(b)). STABL computations at this condition show second-mode waves with a peak frequency of 108 kHz at x= 0.376 m and an N factor of 1.8, in reasonable agreement with the experiments. First-mode waves have an estimated N factor of 0.3 at a frequency of 48 kHz and wave angle of 62 degrees. However, the low growth of these first-mode waves makes the maximum values difficult to identify. Low-frequency disturbances preceding the formation of the second-mode waves are not observed in HWT-14 and would not be expected because of the low first-mode N factors.

At Mach 14, the structure of the wave packet does not change much in subsequent schlieren images. This slow change with downstream distance is also seen in the pressure measurements and in the frequency content in the PSD's. The waves also have a much larger spanwise coherence compared to Mach 5 and 8 (Fig. 21). This is expected because of the thicker boundary layer at Mach 14.

The results from Mach 5, 8, and 14 can be qualitatively compared near this Re to study Mach-number effects on transition. The boundary layer in HWT-5 was completely laminar over the schlieren viewing area (Fig. 4). Measurements in HWT-8 showed the presence of small second-mode waves (Fig. 12). A second harmonic was just beginning to develop in the pressure spectra. In HWT-14, intermittent second-mode waves were observed and showed two nonlinear harmonics (Fig. 19).

Despite the similar Re, it is difficult to make direct comparisons between the different tunnels. The wall temperature ratio is varying between the tunnels, which affects the stability of the boundary layer. This wall temperature ratio decreases from about 0.7 at Mach 5 to 0.3 at Mach 14. The boundary-layer stability also changes; the maximum N factors for both the first and second-mode change at each M. Also, the tunnel noise is varying between the different tunnels. The integrated noise between 0–50 kHz as measured by Kulite

pressure sensors is 2 % at Mach 5 and 5 % at Mach 8 near this Re. It is expected that the noise levels are even higher at Mach 14, though no measurements of the noise have been made. Table 3 summarizes the difference between these conditions. Future work should try to make sense of these differences and the resulting characteristics of transition on the cone at varying M.

Table 3. Comparison of the Sandia Hypersonic Wind Tunnels.

M	$Re \times 10^6/m$	T_w/T_{aw}	Maximum second-mode N factor at x = 0.376 m	Maximum first-mode N factor at x = 0.376 m	Noise Level (%)
4.95	4.39	0.69	2.2	1.5	1
7.8	3.62	0.44	4.1	0.6	5
14.4	3.44	0.34	1.8	0.3	?

D. Cone Vibration Measurements

An additional experiment was conducted to begin looking at coupled fluid-structure interactions caused by the transitional pressure fluctuation loading. Accelerometers were placed on the model, sting support, and tunnel in order to study any flow-induced vibration of the model. A Kulite pressure transducer was also used to measure the base pressure of the cone. An interesting observation was made at Mach 5 at a low Re of $4.39 \times 10^6/m$. As discussed in Section A, the boundary layer along most of the cone is laminar at this Re. Occasional wave packets are observed near the end of the cone at x = 0.452 m. Fig. 22 shows time traces from two PCB132 sensors in the spanwise array at this location. Higher pressure fluctuations are observed near t = 0.096 and 0.15 s which correspond to the passage of second-mode wave packets. When these packets are observed, a corresponding decrease in the base pressure of the model is seen. It appears that the boundary-layer disturbances change the wake of the model as they leave the cone surface, resulting in base pressure fluctuations.

Fig. 23 shows the pressure traces and corresponding power-spectral densities from the base Kulite pressure transducer over a range of Re. A large low-frequency component is observed at the lowest freestream Reynolds numbers, corresponding to this base pressure oscillation. At higher Re, these low frequencies disappear, likely because the boundary layer is predominately turbulent over the base of the model. Unfortunately, the model was not run at lower Re to see if these low-frequencies would also disappear if the boundary-layer is completely laminar at the base of the cone.

These low frequencies might excite vibration of the structure. An accelerometer was placed on the inside of the model base, directly behind the base pressure sensor. When these boundary-layer disturbances leave the cone and the base pressure of the model decreases, higher spanwise and vertical accelerations seem to be excited (Fig. 22). These higher vibrations take much longer to die out than the input pressure fluctuations, but appear to be correlated. Unfortunately at higher Re, there are many more boundary-layer disturbances generated by the end of the cone. This leads to continuous excitation of the base accelerometer and prevents isolated bursts of increased acceleration from being observed and correlated with the pressure traces.

In HWT-8, the base Kulite pressure fluctuations show a low-frequency peak and elevated fluctuations at lower Re (Fig. 24). In HWT-14, no large low-frequency peak is observed (Fig. 25). However in both cases, no large oscillations in the mean pressure are observed as was seen in HWT-5. Also, there are no distinctive peaks in the base acceleration that can be readily correlated with the pressure traces. This is likely because too many disturbances are generated by the end of the cone in HWT-8 and 14, even at these low Re. These many disturbances again create continuous vibration of the base accelerometer.

The correlation between the occurrence of wave packets and higher base acceleration still needs to be investigated further. In the current setup, the last pressure sensors on the cone are 0.065 m upstream of the base of the cone. This offset allows many more wave packets and turbulent spots to develop before the end of the model. Also, the spanwise array of sensors only covers 80 degrees of the circumference. The state of the boundary layer around the remainder of the cone is unknown. Any additional disturbances around the circumference will also contribute to structural excitation. In future experiments, it would be useful to have schlieren imaging of the base of the cone as well as a higher frequency PCB132 sensors around the cone circumference and on the base of the model. This will allow the state of the boundary layer at the end of the cone to be better characterized and correlated to base vibration. Tests should also be run at lower Re or with a shorter model in order to have a more laminar boundary layer at the end of the cone.

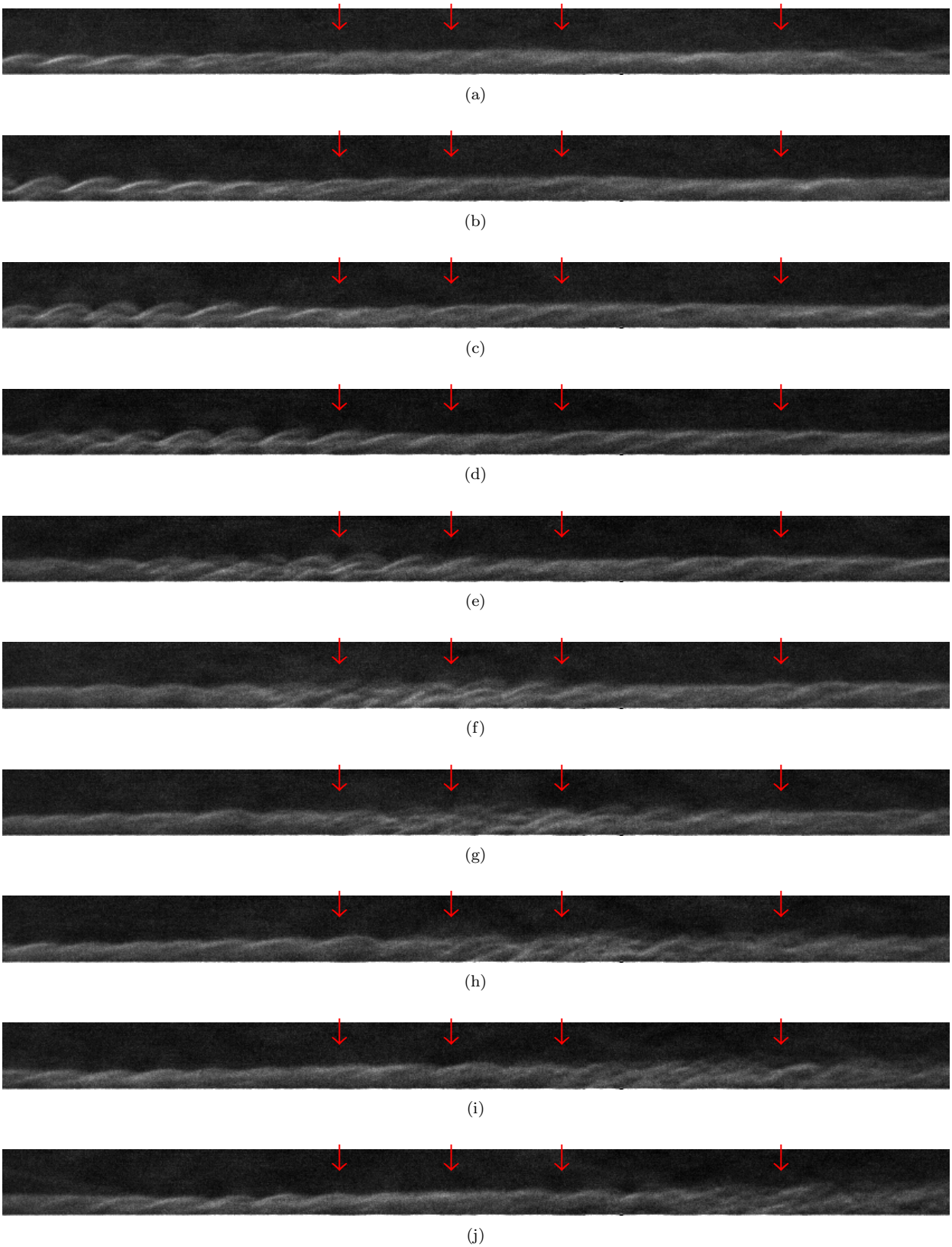

(a)

(b)

(c)

(d)

(e)

(f)

(g)

(h)

(i)

(j)

Figure 15. Schlieren images showing intermittent disturbances within mostly second-mode waves, HWT-8, $t = 1.263 - 1.362\ ms$, $f = 91\ kHz$, $Re = 7.08 \times 10^6/m$, $M = 7.84$, $P_0 = 2429\ kPa$, $T_0 = 610\ K$.

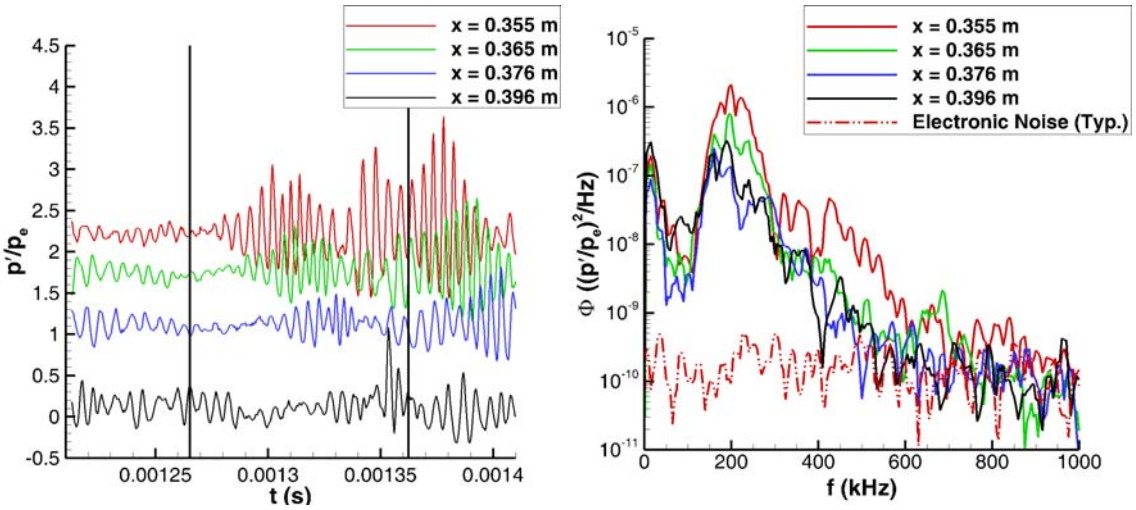

(a) (b)

Figure 16. Simultaneous pressure measurements, HWT-8, $Re = 7.08 \times 10^6/m$, $M = 7.84$, $P_0 = 2429\ kPa$, $T_0 = 610\ K$ **(a) Pressure traces, each trace is vertically offset proportional to x. Vertical black lines mark the time of the corresponding schlieren images; (b) Power-spectral densities.**

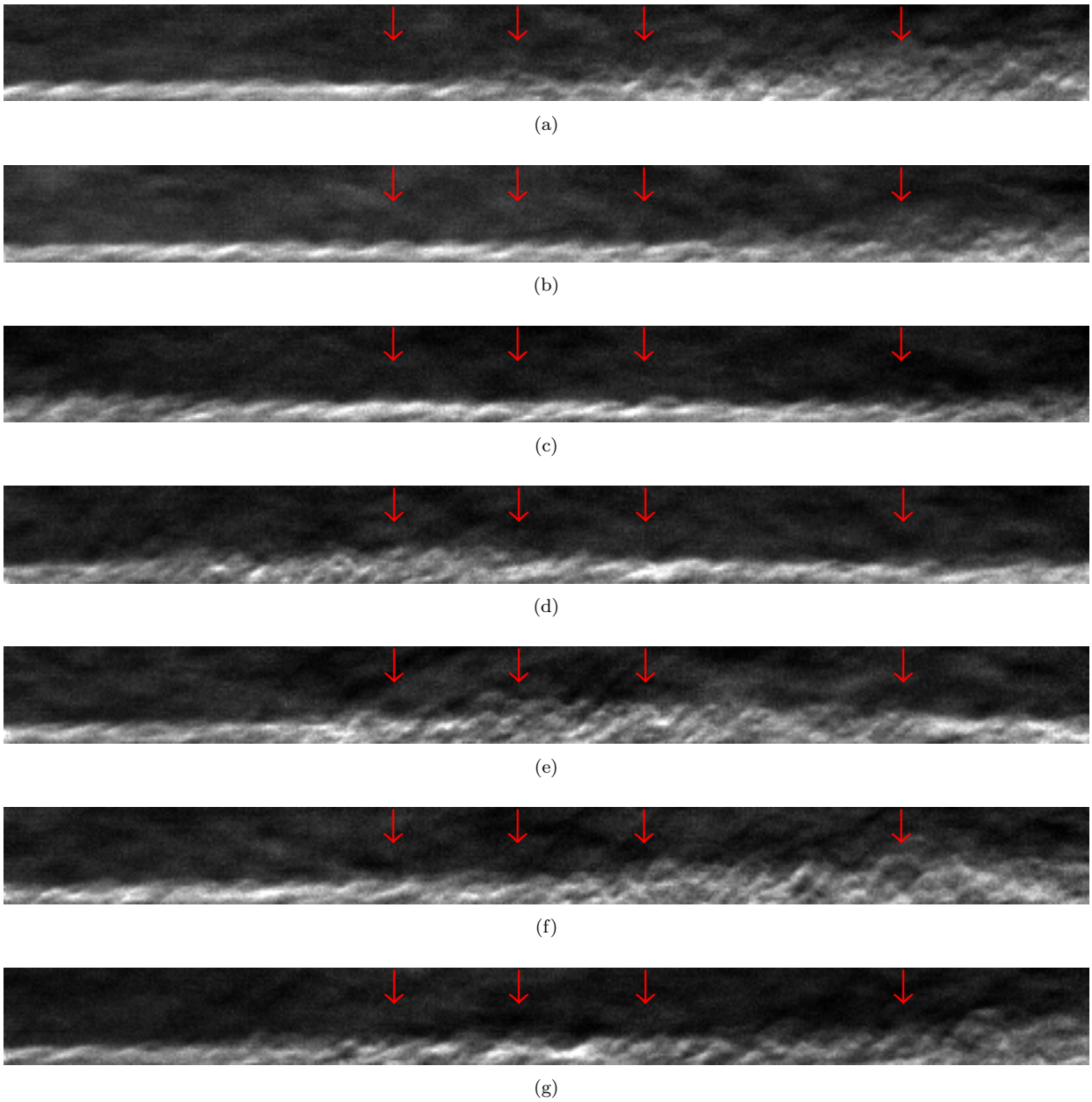

(a)

(b)

(c)

(d)

(e)

(f)

(g)

Figure 17. Schlieren images showing intermittent disturbances, HWT-8, $t = 1.180 - 1.326\ ms$, $f = 205\ kHz$, $Re = 9.74 \times 10^6/m$, $M = 7.87$, $P_0 = 3338\ kPa$, $T_0 = 611\ K$**. Every fifth image of the schlieren movie is shown.**

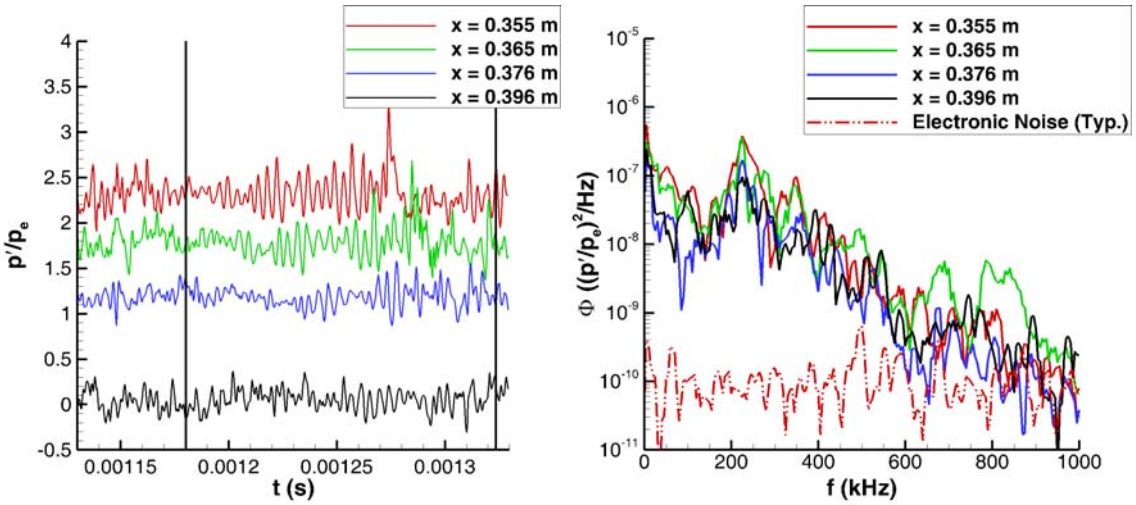

(a) (b)

Figure 18. Simultaneous pressure measurements, HWT-8, $Re = 9.74 \times 10^6/m$, $M = 7.87$, $P_0 = 3338\ kPa$, $T_0 = 611\ K$ **(a) Pressure traces, each trace is vertically offset proportional to x. Vertical black lines mark the time of the corresponding schlieren images; (b) Power-spectral densities.**

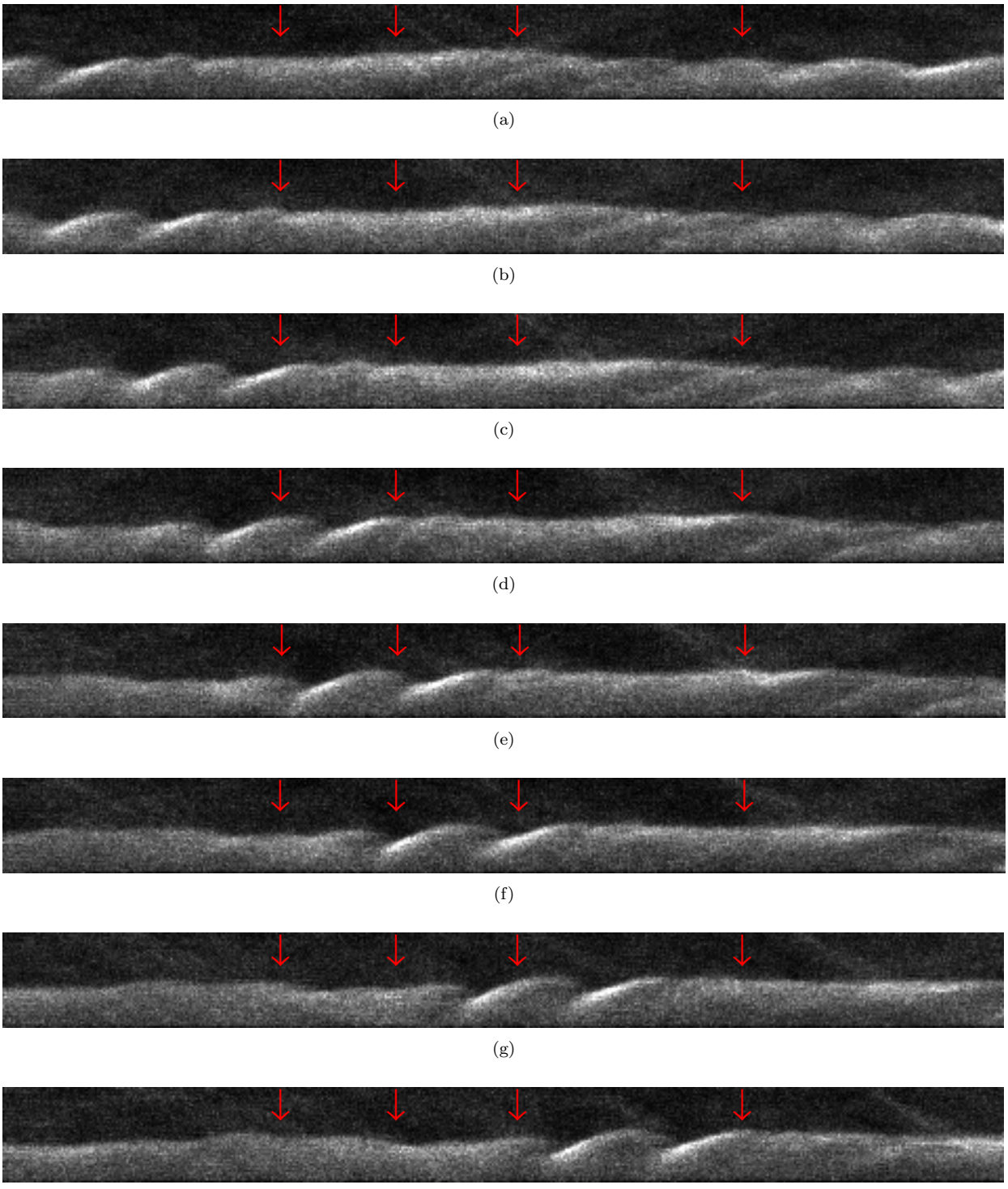

(a)

(b)

(c)

(d)

(e)

(f)

(g)

(h)

Figure 19. Schlieren images showing intermittent wave packets, HWT-14, $t = 0.525 - 0.560ms$, $f = 200\ kHz$, $Re = 3.44 \times 10^6/m$, $M = 14.4$, $P_0 = 16.2\ Mpa$, $T_0 = 1075\ K$.

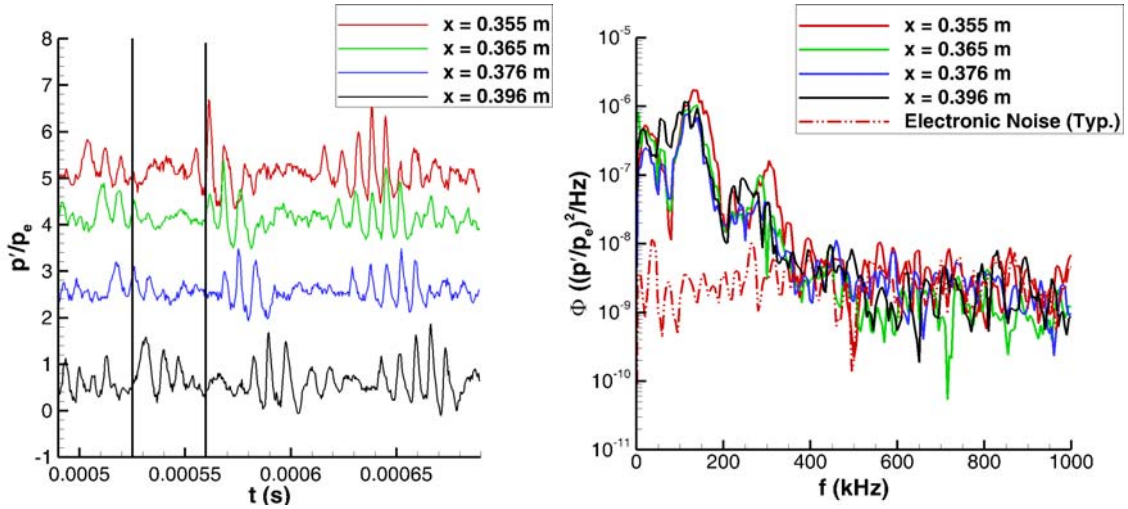

(a) (b)

Figure 20. Simultaneous pressure measurements, HWT-14, $Re = 3.44 \times 10^6/m$, $M = 14.4$, $P_0 = 16.2\ Mpa$, $T_0 = 1075\ K$ **(a) Pressure traces, each trace is vertically offset proportional to x. Vertical black lines mark the time of the corresponding schlieren images; (b) Power-spectral densities.**

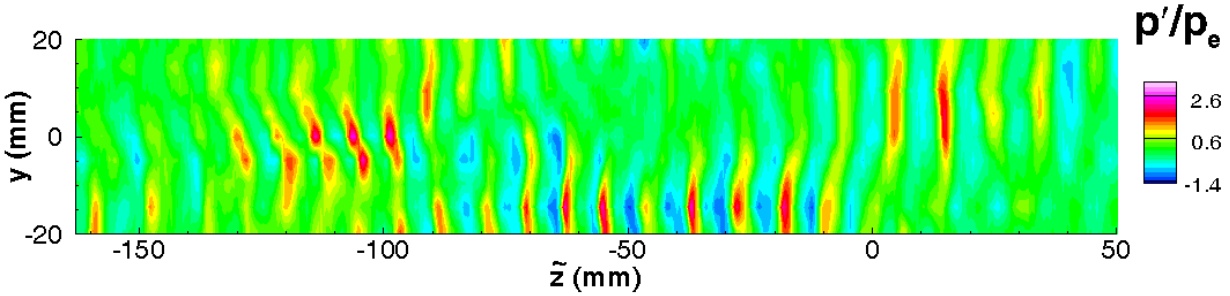

Figure 21. Contour plot showing intermittent wave packets, HWT-14, $Re = 3.44 \times 10^6/m$, $M = 14.4$, $P_0 = 16.2\ Mpa$, $T_0 = 1075\ K$.

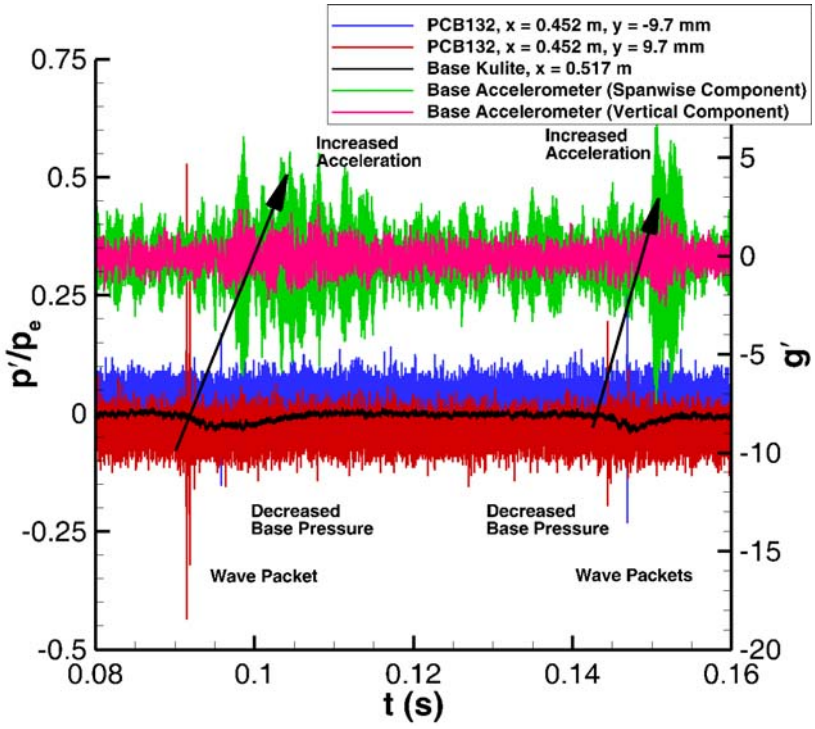

(a)

Figure 22. Simultaneous PCB132 pressure measurements in the spanwise array at x = 0.452, Kulite base pressure measurements at x = 0.517 m, and base acceleration measurements at x = 0.517 m.

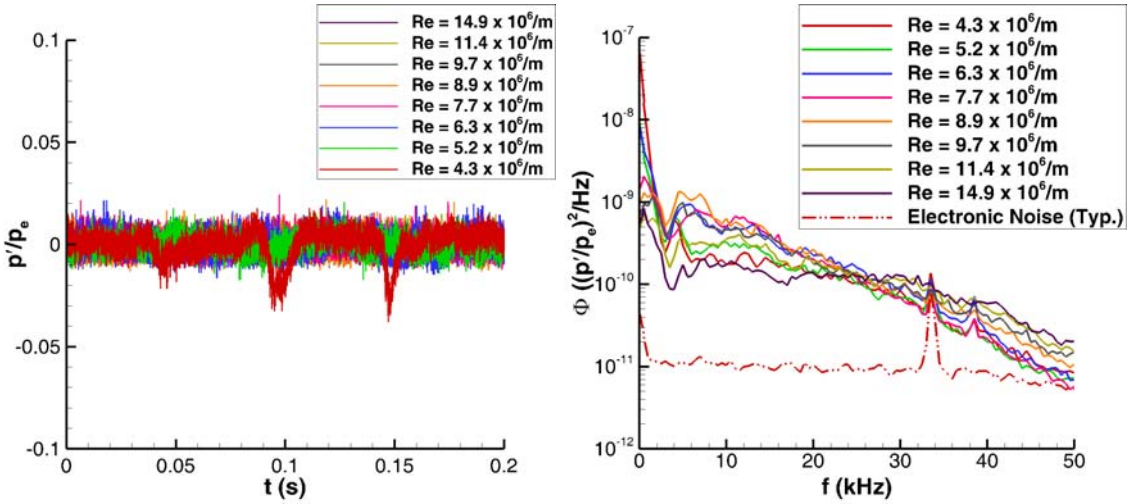

(a) (b)

Figure 23. Kulite base pressure measurements at varying Re, HWT-5.

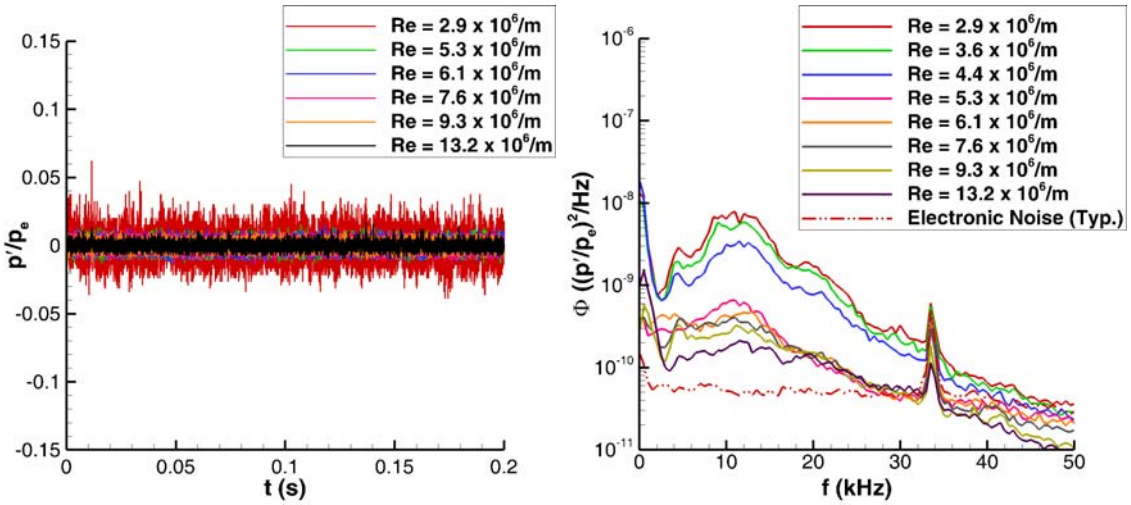

(a) (b)

Figure 24. Kulite base pressure measurements at varying Re, HWT-8.

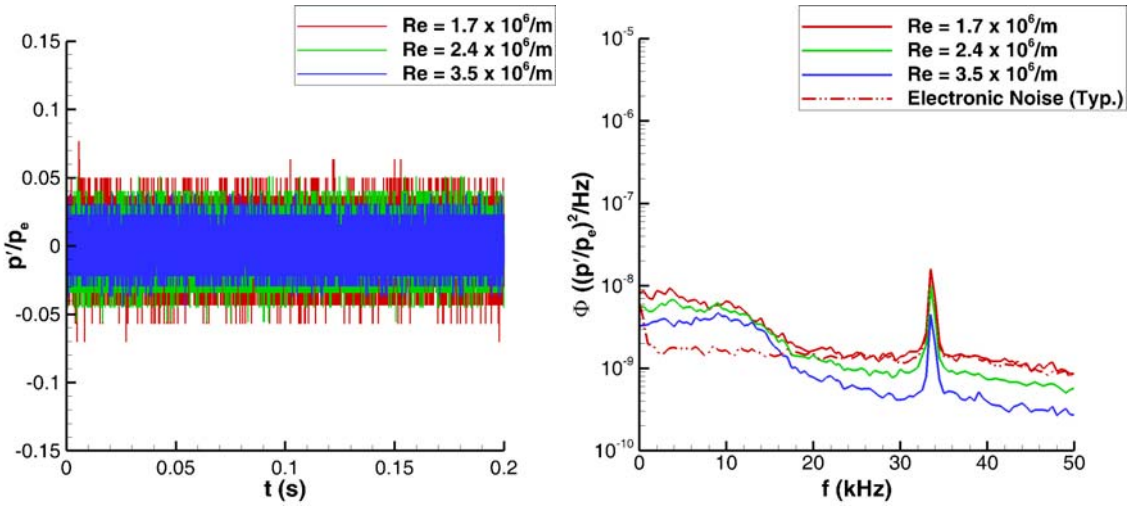

(a) (b)

Figure 25. Kulite base pressure measurements at varying Re, HWT-14.

V. Concluding Remarks

Simultaneous high-frequency pressure and schlieren measurements were made of boundary-layer disturbances in the Sandia Hypersonic Wind Tunnel at Mach 5, 8, and 14 over a range of Re. This allows the intermittent behavior of the boundary layer to be characterized. At Mach 5, low frequency disturbances were intermittently observed in the boundary layer. Higher-frequency wave packets would develop on top of these disturbances and break down into turbulent spots surrounded by an otherwise smooth boundary layer. Boundary-layer stability computations were performed to identify these disturbances. The frequency of the low-frequency disturbances was in agreement with the expected range for first-mode instability waves. However, the most amplified first-mode waves are oblique, and it is unclear how they would show up in the schlieren videos. These low-frequencies also could not be identified in the surface pressure traces. More evidence is needed to conclusively identify these low-frequency disturbances. The higher-frequency disturbances, however, were observed in both the schlieren and surface pressure measurements. The waves showed the characteristic rope-like structure of second-mode waves in the schlieren measurements and the frequency of these waves was in agreement with second-mode stability computations.

At Mach 8, the boundary layer was dominated by second-mode waves. These waves have a very high N factor. Regions of these waves would break down into turbulent spots at higher Re. However, these turbulent spots were surrounded by second-mode waves, not the smooth laminar boundary layer seen at Mach 5. Also, low-frequency disturbances were not observed before the formation of the second-mode waves. At Mach 14, second-mode waves were again observed in both the schlieren videos and time traces. The frequency of these disturbances was in agreement with stability computations. No evidence of low-frequency disturbances was seen prior to the development of the second-mode waves. The maximum Re in HWT-14 is low, so the breakdown of the second-mode waves to turbulent spots did not occur.

In HWT-5, boundary-layer disturbances were seen to excite base vibration of the model. When these boundary-layer disturbances leave the end of the cone, they appear to affect the wake of the model resulting in a decrease in the base pressure. When this occurred, vibration of an accelerometer mounted on the base of the model was excited. This correlation was observed only at low Re at Mach 5. At higher Re and in HWT-8 and 14, too many disturbances were formed by the end of the cone. This lead to continuous acceleration of the base accelerometer, preventing isolated bursts of acceleration from being observed and correlated to the formation of boundary-layer disturbances. Future experiments should explore this base vibration in more detail. This could be an important factor contributing to the vibration of interior components on reentry vehicles in flight.

A lot of data analysis remains to be performed. A quantitative correlation between the surface pressure measurements and the schlieren images still needs to be obtained. Differences in the schlieren and surface pressure measurements should be explored, especially at higher M when an delay seems to occur between when disturbances are seen in the schlieren images and the resulting surface pressure fluctuations. Also, in order to characterize the boundary layer and resulting pressure fluctuations, the boundary-layer intermittency, burst rate, and distribution of burst length on the cone need to be computed. This calculation can be done using both the schlieren images and surface pressure measurements. By combing this statistical information about the disturbance formation with information about the pressure structure and growth properties of the disturbances, the pressure fluctuations at a given location on the cone should be able to be computed. This dataset can then be used to help develop predictive models of a flight vehicle's environment.

References

[1]Laganelli, A. L., Martellucci, A., and Shaw, L. L., "Wall Pressure Fluctuations in Attached Boundary-Layer Flow," *AIAA Journal*, Vol. 21, No. 4, 1983, pp. 495–502.

[2]Pate, S. R. and Brown, M. D., "Acoustic Measurements in Supersonic Transitional Boundary Layers," AEDC-TR-69-182, October 1969.

[3]Johnson, R. I., Macourek, M. N., and Saunders, H., "Boundary Layer Acoustic Measurements in Transitional and Turbulent Flow at $M_\infty = 4.0$," AIAA Paper 69-344, April 1969.

[4]Cassanto, J. M. and Rogers, D. A., "An Experiment to Determine Nose Tip Transition with Fluctuating Pressure Measurements," *AIAA Journal*, Vol. 13, No. 10, October 1975, pp. 1257–1258.

[5]Martellucci, A., Chaump, L., Rogers, D., and Smith, D., "Experimental Determination of the Aeroacoustic Environment about a Slender Cone," *AIAA Journal*, Vol. 11, No. 5, 1973, pp. 635–642.

[6]Pate, S. R., "Dominance of Radiated Aerodynamic Noise on Boundary-Layer Transition in Supersonic/Hypersonic Wind Tunnels," AEDC-TR-77-107, March 1978.

[7]Johnson, C. B., Stainback, P. C., Wicker, K. C., and Boney, L. R., "Boundary-Layer Edge Conditions and Transition Reynolds Number Data for a Flight Test at Mach 20 (Reentry F)," NASA TM X-2584, July 1972.

[8]Narasimha, R., "The Laminar-Turbulent Transition Zone in the Boundary Layer," *Progress in Aerospace Sciences*, Vol. 22, January 1985, pp. 29–80.

[9]Park, S. and Lauchle, G., "Wall Pressure Fluctuation Spectra Due to Boundary-Layer Transition," *Journal of Sound and Vibration*, Vol. 319, 2009, pp. 1067–1082.

[10]Casper, K. M., *Hypersonic Wind-Tunnel Measurements of Boundary-Layer Pressure Fluctuations*, Master's Thesis, Purdue University, School of Aeronautics & Astronautics, August 2009.

[11]Casper, K. M., Beresh, S. J., Henfling, J. F., Spillers, R. W., Pruett, B. O. M., and Schneider, S. P., "Hypersonic Wind-Tunnel Measurements of Boundary-Layer Pressure Fluctuations," AIAA Paper 2009-4054, June 2009.

[12]Alba, C. R., Casper, K. M., Beresh, S. J., and Schneider, S. P., "Comparison of Experimentally Measured and Computed Second-Mode Disturbances in Hypersonic Boundary-Layers," AIAA Paper 2010-897, January 2010.

[13]Casper, K. M., Beresh, S. J., Henfling, J. F., Spillers, R. W., and Pruett, B. O. M., "High-Speed Schlieren Imaging of Disturbances in a Transitional Hypersonic Boundary Layer," AIAA Paper 2013-0376, January 2013.

[14]Casper, K., Beresh, S., and Schneider, S., "Characterization of Controlled Perturbations in a Hypersonic Boundary Layer," AIAA Paper 2012-281, January 2012.

[15]Beresh, S. J., Henfling, J. F., Spillers, R. W., and Pruett, B. O. M., "Fluctuating Wall Pressures Measured beneath a Supersonic Turbulent Boundary Layer," *Physics of Fluids*, Vol. 23, 075110, 2011.

[16]Berridge, D. C., *Measurements of Second-Mode Instability Waves in Hypersonic Boundary Layers with a High-Frequency Pressure Transducer*, Master's Thesis, Purdue University School of Aeronautics & Astronautics, December 2010.

[17]Ward, C. A. C., Wheaton, B. M., Chou, A., Berridge, D. C., Letterman, L. E., Luersen, R. P. K., and Schneider, S. P., "Hypersonic Boundary-Layer Transition Experiments in the Boeing/AFOSR Mach-6 Quiet Tunnel," AIAA Paper 2012-0282, January 2012.

[18]Johnson, H. B., *Thermochemical Interactions in Hypersonic Boundary Layer Stability*, Ph.D. Thesis, University of Minnesota, 2000.

[19]Johnson, H. B. and Candler, G. V., "Hypersonic Boundary Layer Stability Analysis Using PSE-Chem," AIAA Paper 2005-5023, June 2005.

[20]Taylor, G. I., "The Spectrum of Turbulence," *Proceedings of the Royal Society of London*, Vol. 164, 1938, pp. 476–490.

[21]Dennis, D. J. C. and Nickels, T. B., "On the Limitations of Taylors Hypothesis in Constructing Long Structures in a Turbulent Boundary Layer," *Journal of Fluid Mechanics*, Vol. 614, 2008, pp. 197–206.

[22]Kimmel, R. L., Demetriades, A., and Donaldson, J., "Space-Time Correlation Measurements in a Hypersonic Transitional Boundary Layer," AIAA Paper 95-2292, June 1995.

[23]Demetriades, A., "Hypersonic Viscous Flow Over a Slender Cone Part III Laminar Instability and Transition," AIAA Paper 1974-535, June 1974.